scientific reports

Check for updates

OPEN

Evaluation of Dy–Cr integration in MOF/rGO nanocomposite for enhanced electrochemical water splitting

Khadija-tul-Kubra[1], Faiqa Noreen[1], Ali Junaid[1], Saif Ullah[1], Syed Imran Abbas Shah[1]✉, Abdullah K. Alanazi[2], Magdi E. A. Zaki[3], Sobhi M. Gomha[4]✉, Aymen Shahsawar[1], Mohamed A. Salem[5] & Zahid Shafiq[1]✉

The development of stable, cost-effective electrocatalysts for water splitting is critical for enhancing hydrogen energy systems, particularly for the hydrogen evolution reaction (HER) and the oxygen evolution reaction (OER). Metal-organic frameworks (MOFs) show great promise due to their tunable structures, high surface areas, and ability to optimize active sites for both HER and OER, improving catalytic efficiency. This study synthesizes a composite material of dysprosium–chromium MOF and reduced graphene oxide (Dy–Cr-MOF/rGO) through a simple hydrothermal method. The Dy–Cr-MOF/rGO composite exhibited exceptional electrocatalytic performance, achieving an OER overpotential of 164 mV and HER overpotential of 158 mV, with Tafel slopes of 42 mV dec^{-1} and 32 mV dec^{-1}, respectively. After 50 h of continuous operation in a two-electrode system, the composite maintained stable Tafel slopes of 108 mV dec^{-1} (OER) and 87 mV dec^{-1} (HER). Practical device tests further confirmed the stability and robustness of the composite, highlighting its potential for scalable applications in electrochemical energy conversion systems. These results demonstrate that Dy–Cr-MOF/rGO is a promising bifunctional electrocatalyst for efficient water splitting.

Keywords Dy–Cr-MOF/rGO nanocomposite, Bifunctional electrocatalysts, Electrochemical water splitting, Electrochemical performance

Environmental issues like global warming, air pollution, and health problems caused by fossil fuels require a change to new forms of energy and sustainable energy sources[1]. Hydrogen fuel, with a combustion value of 142 MJ/kg and a value is flexible, eco-friendly and, more importantly, is a carbon-free energy source. Hydrogen produces only water vapor and is combusted safely; there are no toxic fossil fuel carbon emissions[2–4]. The potential of water splitting for hydrogen production is limited by the complex four-proton/four-electron exchange at the OER, which involves high energy costs and significant overpotential, ultimately reducing the efficiency of water splitting[5–7].

It is essential to develop high-performing OER electrocatalysts with low overpotentials (0.2 to 0.4 V) to enhance hydrogen generation and energy conversion efficiency[8]. MOFs have recently shown potential to fill this need because of their inexpensive raw materials, straightforward manufacturing, high surface area, stability, and proficient conductivity. The special features of MOFs, primarily their tunable composition and porosity, allow for their considerable efficiency as electrocatalysts for water splitting[9,10]. While the iridium (Ir), ruthenium (Ru) and platinum (Pt) are examples of noble metals which possess high catalytic activity, but their high cost, limited availability and tendency to degrade challenge their use[11,12]. Presence of transition metals (iron, copper, cobalt, nickel, and chromium) in MOFs and their abundant active centers significantly enhance electrochemical performance. Chromium (Cr) is involved in these because of his great catalytic activity, high conductance, and varying oxidation states (Cr^{+2}, Cr^{+3}, Cr^{+6}) which exist in acid and alkaline solutions, along

[1]Institute of Chemical Sciences, Bahauddin Zakariya University, Multan 60800, Pakistan. [2]Department of Chemistry, College of Science, Taif University, Taif, Saudi Arabia. [3]Department of Chemistry, Faculty of Science, Imam Mohammad Ibn Saud Islamic University (IMSIU), 11623 Riyadh, Saudi Arabia. [4]Department of Chemistry, Faculty of Science, Islamic University of Madinah, 42351 Madinah, Saudi Arabia. [5]Health Specialties, Basic Sciences and Their Applications Unit, Applied College, Muhayl Asir, King Khalid University, 62529 Abha, Saudi Arabia. ✉email: ; smgomha@iu.edu.sa; zahidshafiq@bzu.edu.pk

with his multiple oxidation states, conductivity, and active catalytic nature[13]. Moreover, dysprosium (Dy) enhances charge transfer and electron mobility with its unique electronic architecture, exceptional corrosion resistance, and unique electron structure[14,15]. Using carbon materials like reduced graphene oxide (rGO) can greatly increase the catalytic activity of MOFs. Because rGO has a high surface area and great conductivity and can be versatile rGO improve the electrocatalytic performance of both the oxygen evolution reaction (OER) and the hydrogen evolution reaction (HER)[16,17]. Because of the improvement of active site accessibility and more efficient electron transfers, rGO composites efficiency has been increased[18]. Dysprosium (Dy) and Chromium (Cr) play complementary roles in the bimetallic MOF, enhancing electrocatalytic performance. Dy, with its high electro positivity and stable + 3 oxidation state, contributes to electron donation and stabilizing active sites, while Cr, with its variable oxidation states (Cr^{3+} and Cr^{6+}), facilitates redox reactions and optimizes the adsorption of reactants. The incorporation of Dy into the MOF structure introduces unique electronic properties, including its stable + 3 oxidation state and distinct coordination chemistry, which enhance both catalytic activity and stability compared to typical MOF/rGO or bimetallic MOF systems. Dy-based MOFs demonstrate improved electrochemical performance, offering lower overpotentials and enhanced stability for both HER and OER, which surpasses the performance of many existing catalysts in literature. Recent advancements in bifunctional catalysts for water splitting have demonstrated significant progress. Sun et al. developed porous iron and chromium co-doped cobalt phosphide nanosheets, achieving low overpotentials of 103.7 mV for HER and 256.4 mV for OER in alkaline media at 10 mA cm^{-2}[19]. Ma et al. synthesized dysprosium-doped Fe-MOF with a hydrangea flower-like nanostructure, achieving an overpotential of 258 mV for OER and surpassing RuO_2[20]. Narwade et al. created Ni/NiO@rGO, which showed minimal overpotentials of 582 mV for HER and 480 mV for OER with Tafel slopes of 63 mV dec^{-1} (HER) and 41 mV dec^{-1} (OER)[20]. Y.Ma et al. designed Ni-Co MOF@rGO, which exhibited excellent bifunctional activity with a ΔE of 1.02 V in 0.1 M KOH[21].

In this study, we fabricated the Dy–Cr-MOF/rGO nanocomposite, a novel material synthesized hydrothermally for efficient electrochemical water splitting. The Dy–Cr-MOF/rGO composite creates several oxygen vacancies, significantly increasing the active surface area to 285 cm^2. This increase in surface area contributes to low overpotentials of 164 mV for OER and 158 mV for HER, along with reduced Tafel slopes of 42 mV dec^{-1} and 32 mV dec^{-1}, respectively. The composite also demonstrates low charge transfer resistance (Rct) values of 5.77 Ω for OER and 816.54 Ω for HER in 1.0 M KOH solution. Covalent interactions between MOF and rGO further enhance the electrocatalytic activity, making the Dy–Cr-MOF/rGO nanocomposite a promising material for efficient water splitting applications.

Experimental

Chemicals and reagents

Dysprosium Chloride hexahydrate ($DyCl_3{\cdot}6H_2O$, 99.0%), Benzene tricarboxylic acid ($C_9H_6O_6$, BTC, 98%, Sigma Aldrich) Chromium nitrate hexahydrate ($Cr(NO_3)_3{\cdot}6H_2O$, 98%, Sigma Aldrich) as a metal precursor. N, N-dimethylformamide (DMF), and ethanol (C_2H_5OH as a solvent, Sodium acetate (99%, CH_3COONa, Sigma Aldrich), graphite powder (99%, Merck), Sulfuric acid (58.5%, H_2SO_4, Merck), potassium permanganate (97%, $KMnO_4$, Emplura), Hydrogen peroxide (30%, H_2O_2, Merck), Hydrochloric acid (37%, HCl, Merck), Hydrazine (98% N_2H_4, Sigma Aldrich), ethanol (99%, C_2H_5OH, Sigma Aldrich) and distilled water were obtained from China Medicine. Since every reagent was of analytical variety, no additional purification was necessary.

Synthesis of Dy-MOF

Dy-MOF was synthesized via a solvothermal method. Dysprosium chloride hexahydrate ($DyCl_3{\cdot}6H_2O$, 1.507 g, 4 mmol) and benzene-1,3,5-tricarboxylic acid (BTC, 0.315 g, 1.5 mmol) were sequentially dissolved in 100 mL of N, N-dimethylformamide (DMF) under continuous stirring for 30 min. The resulting homogeneous solution was transferred to a 150 mL Teflon-lined stainless-steel autoclave, sealed, and heated at 160 °C for 12 h. After natural cooling to room temperature, the precipitate was collected by filtration, washed twice with fresh DMF to remove unreacted BTC, and subsequently rinsed with anhydrous ethanol and deionized water (3 × 30 mL each) to eliminate residual impurities. The final product was dried at 150 °C for 10 h under vacuum to yield Dy-MOF powder.

Synthesis of Cr-MOF

Firstly, (1.6 g, 0.04 M) chromium nitrate hexahydrate and (0.315 g, 0.015 M) of benzene tricarboxylic acid were sequentially added to a 100 mL solution of DMF. The mixed solution underwent stirring for 30 min before being transferred to a hydrothermal reactor that was lined with Teflon. The reactor was sealed and placed in the furnace, where it was heated to 160 °C for 12 h. The sample was filtered and dried for 5 h at 150 °C. To remove any unreacted BTC, the sample was washed twice in a DMF solution. The product was then washed in a two-step process, first using anhydrous ethanol and then using deionized water, to remove any remaining surface impurities. Finally, the removal of residual ethanol, water, and other impurities was accomplished by drying at 150 °C for 10 h, completing the synthesis of Cr-MOF.

Synthesis of Dy–Cr-MOF

In the procedure, (0.63 g, 0.03 M) of benzene tricarboxylic acid was dissolved 100 mL of DMF. Then, (1.507 g, 0.04 M) of $Dy(NO_3)_2{\cdot}6H_2O$ and (1.6 g, 0.04 M) of $Cr(NO_3)_3{\cdot}6H_2O$ were added and stirred for 1 h. Which was then placed in a Teflon-lined autoclave. The autoclave was sealed and kept at 160 °C for 12 h. The products were collected, washed, and cooled to room temperature Scheme 1. The resulting products were named Dy–Cr-MOF.

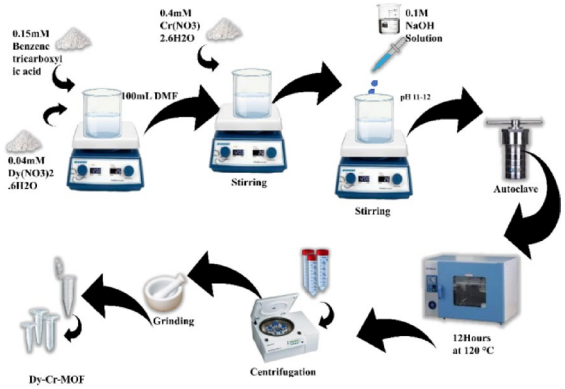

Scheme 1. Synthesis of Dy–Cr-MOF.

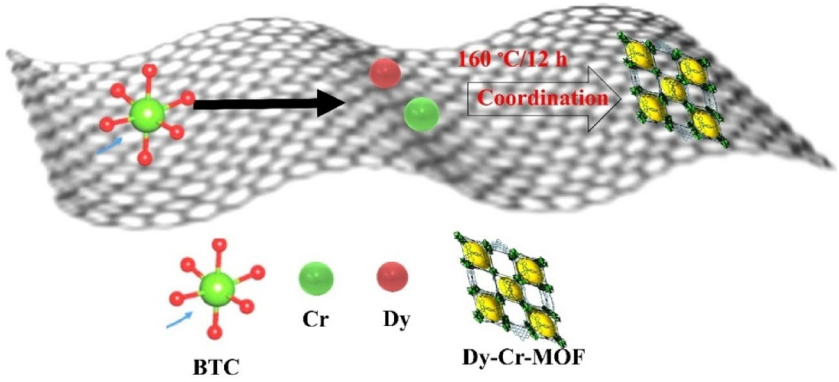

Scheme 2. Synthesis of Dy–Cr-MOF/rGO.

Synthesis of rGO

The synthesis of graphene oxide (GO) is carried out by a modified Hummer's method. Initially, a mixture of 3 g of graphite powder with 69 mL of sulfuric acid is prepared. Then 9 g of $KMnO_4$ are added slowly while temperature is maintained below 20 °C. The resultant mixture is stirred and held at 35 °C for 45 min before 150 mL of distilled water is added. The addition of water will cause a vigorous and vicious reaction, increasing the temperature to 100 °C. The addition of 30 mL of 30% H_2O_2 with 500 mL of distilled water will initiate the reaction and yield a yellow suspension. The suspension is then filtered during the precipitation and drying step to remove metal left in the suspension, which was done by 750 mL of a 1:10 HCl solution. The precipitation will then be dried at 60 °C then clumped and dispersed in distilled water for gentle stirring for 2–3 h. The suspension is then distilled, and water is added with a 7–9 day period to achieve neutral pH. The material is sonicated, centrifuged to remove residual GO, and dried at 60 °C for one hour. For rGO, 100 mg of graphite oxide is added to 250 mL distilled water, creating a yellow-brown suspension. The mixture is sonicated until clear. Then, 1 mL of hydrazine hydrate is added, and the mixture is heated in an oil bath at 100 °C for 24 h, forming a black precipitate. After filtration, the product is washed with distilled water and methanol, then dried at room temperature to yield rGO.

Synthesis of Dy–Cr-MOF/rGO

Graphene oxide was synthesized initially using a modified Hummers method, subsequent to a high-temperature process in order to obtain reduced graphene oxide (rGO), as previously detailed Scheme 2. A solution was formulated by merging ethanol with DMF in equal ratio of 40 ml.

The solution was stirred, and then 25 mg of as prepared rGO was dispersed into the solution using ultra sonication. Benzene tricarboxylic acid ($C_9H_6O_6$), $DyCl_3.6H_2O$ (0.1 M), and Cr $(NO_3)_3.6H_2O$ (0.1 M) were introduced separately into the solution, and solution was stirred continuously for 30 min to ensure effective incorporation of Dy and Cr ions. The obtained mixture was transferred to autoclave and then kept in an oven at 160 °C for 8 h. The final product was subjected to three washes with ethanol via centrifugation at 8000 rpm and subsequently dried overnight.

Electrode preparation

The electrochemical measurements were performed in a standard three-electrode configuration using a platinum (Pt) wire as the counter electrode, Ag/AgCl (3 M KCl) as the reference electrode, and catalyst-coated nickel foam (NF, 2 cm × 2 cm) as the working electrode. Prior to coating, NF was sequentially cleaned by sonication

in acetone, 2 M HCl, deionized water, and ethanol for 15 min each, followed by drying at 60 °C for 30 min. To ensure uniform catalyst deposition and reproducible active material loading, 5 mg of the as-synthesized catalyst (rGO, Cr-MOF, Dy-MOF, Dy–Cr-MOF, or Dy–Cr-MOF/rGO) was dispersed in a mixture of 800 µL ethanol, 150 µL deionized water, and 50 µL of 5 wt% Nafion solution, followed by sonication for 30 min to form a homogeneous ink. An aliquot of 200 µL of this ink was drop-cast onto the pre-cleaned NF and dried at 60 °C for 12 h under vacuum, yielding a uniform catalyst loading of 0.5 mg cm^{-2}.

Physical characterization

To measure the Kα discharge in the 2θ range of 10–70° we utilized a Bruker D2 PHASER powdered diffractometer running at a current of 10 mA and voltage of 30 kV. The crystalline and structural characteristics of the hydrothermal produced Cr-MOF, Dy–Cr-MOF, Dy–Cr-MOF, and Dy–Cr-MOF/rGO nanocomposite were validated by XRD. Brunauer-Emmett-Teller (BET; Nova 2200e Qanta Chrome) analysis was applied to ascertain the surfaces area of the materials. The analyzer was designed to run on nitrogen as the adsorbate at 77 K. Exteriors of the materials' morphological behavior were investigated by Czech Republic researchers using a scanning electron microscope (TESCAN MIRA3). The infrared spectra of molecules within the 600–4000 cm^{-1} range were investigated using an Agilent spectrometer (Cary 360, FTIR, Malaysia).

Electrochemical activity

Conventional electrochemical water splitting was investigated in an Ag/AgCl as reference and Platinum wire used as the counter electrode and an electrocatalyst coated on the working electrode in an electrochemical workstation (Corrtest CS350) under 1.0 molar KOH. Under room temperature with a sweeping rate (10 mVs^{-1}), we performed cyclic voltammetry and linear sweep voltammetry using a 1.0 M KOH electrolyte. Using Eq. (1), the resulting potential in Ag/AgCl was then transformed to RHE.

$$E_{RHE} = E_{Ag/Agcl} + 0.197 + (0.059 * pH) \tag{1}$$

E Ag/AgCl denotes potential measured by the Ag/AgCl electrode; Eo indicates absolute thermodynamic potential of the typical Ag/AgCl electrode, equal 0.197 V. For the pH of the electrolyte originally utilized, the value of 0.059 provides the suitable factor.

The overpotential (η) is computed with reference to the given equation.

The following equation is used to calculate the overpotential (η).

$$\eta = E_{RHE} - 1.23 \tag{2}$$

The Tafel value was found using the linear section of the CV graph in respect to the overpotential near to the onset potential of OER. Charge transfer process and reaction kinetics were both studied using Tafel slope. It also reveals details about oxygen evolution reaction's rate-limiting stage. Steady flow polarization gradient was taken into consideration by using following formulae to derive Tafel slope:

$$\eta = (\mathrm{a}) + (\mathrm{b}\ \log\ \mathrm{j}) \tag{3}$$

The symbol η represents overpotential, "a" stands for constant, "j" for current density, "b" for the Tafel plot, which is equal to (2.303) RT/nF, R for electron transport coefficient, "n" for total electron quantity, and F for Faraday's constant. The following equations were used to calculate assumed turnover rate of OER and HER, respectively.

$$\mathrm{TOF}\ (\mathrm{OER}) = \frac{1}{4\,x\,F\,x\,m} \tag{4}$$

$$\mathrm{TOF}\ (\mathrm{HER}) = \frac{1}{2\,x\,F\,x\,m} \tag{5}$$

Electrochemical double layer capacitance, or Cdl was used to find the ECSA. The non-Faradaic approach enabled Cdl to be extracted from Cyclic voltammetry plot across a potential range. We then used the following formula to find ECSA.

$$ECSA = \frac{\mathrm{C_{dl}}}{\mathrm{C_{sp}}} \tag{6}$$

$$C_{dl} = \frac{Slope}{2} \tag{7}$$

The mechanisms of water oxidation were computed using EIS calculations; the dynamics of the OER are connected to the EIS values[22]. Because of its strong electrical characteristics and low electron transportation resistance, the semicircle in the lower frequency shows effective OER results. Assessing the long-term durability of the generated MOFs mainly relies on chronoamperometry.

Results and discussion

The XRD patterns confirm the effective synthesis and phase purity of the catalysts. In Fig. 1(b), rGO exhibits a characteristic (002) plane peak at 2θ = 27.61°, indicating a well-ordered crystalline structure, corresponding to

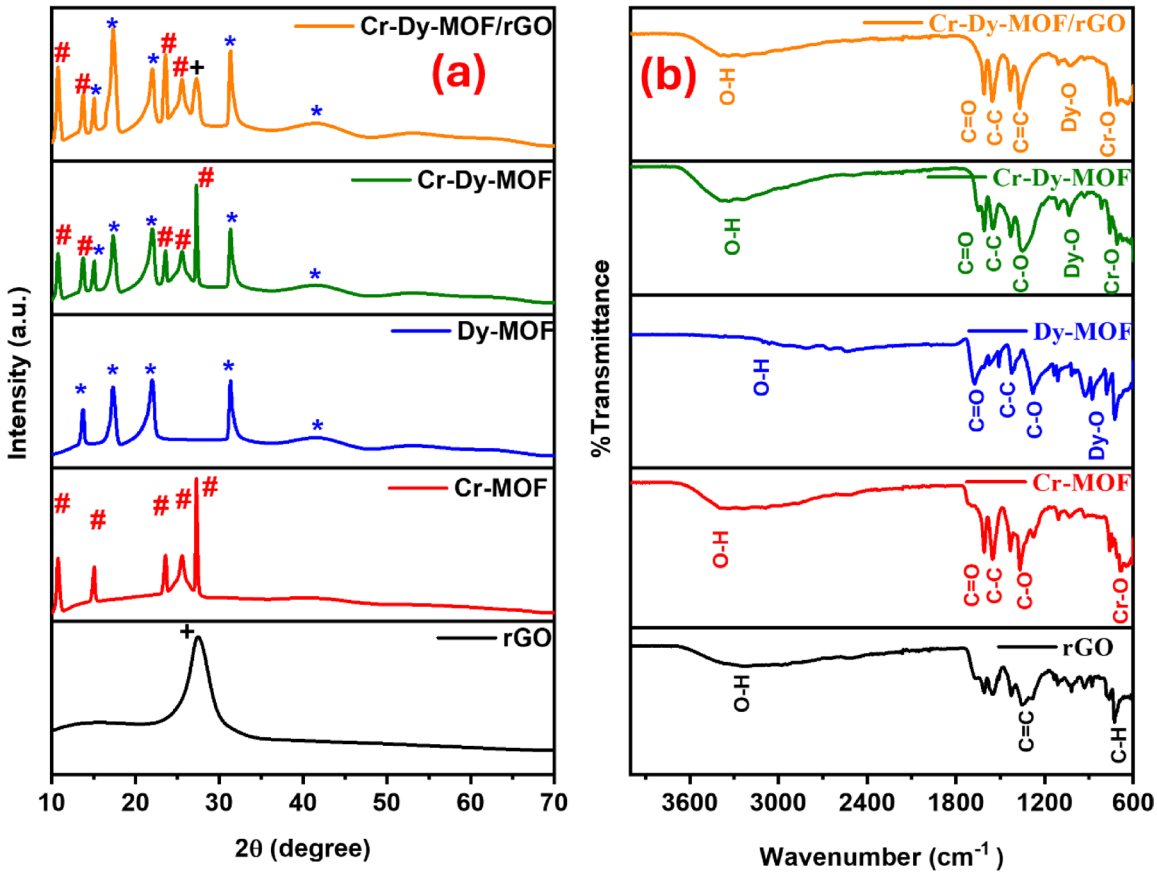

Fig. 1. **a** XRD **b** FTIR graph of rGO, Cr-MOF, Dy-MOF, Dy–Cr-MOF and Dy–Cr-MOF/rGO.

Sr. No.	Material	d-spacing (Å)	Lattice strain	Crystalline Size(nm)	Dislocation density (m-2)
1	rGO	5.31	0.07	1.9	0.27
2	Dy-MOF	4.81	0.15	10.9	6.01
3	Cr-MOF	4.32	0.90	11.5	12.25
4	Dy–Cr-MOF	3.25	1.12	14.7	23.04
5	Dy–Cr-MOF/rGO	2.76	1.24	23.8	43.38

Table 1. Calculated XRD parameters for rGO, Dy-MOF, Cr-MOF, Dy–Cr-MOF and Dy–Cr-MOF/rGO.

the JCPDS card number 00–001-0640. Dy-MOF exhibits diffraction peaks at 13.71°, 17.41°, 21.92°, 31.42°, and 41.92°, confirming its crystalline nature[23]. Cr–MOF shows peaks at 10.76°, 15.13°, 23.49°, 25.53°, and 27.25°, supporting its phase purity[24]. The Dy–Cr-MOF pattern displays peaks at 10.96°, 13.62°, 15.15°, 17.28°, 22.14°, 23.52°, 25.57°, 27.27°, 31.39°, and 41.94°, indicating formation of a bimetallic framework. In Dy–Cr-MOF/rGO composite, peaks at 10.67°, 13.72°, 15.09°, 17.32°, 22.05°, 25.51°, 27.35°, 31.64°, and 42.95° reveal effective incorporation of rGO, with slight peak shifts indicating strong interfacial interactions. This indicates that the crystalline and structural stability of the materials improves and is repetitive for the electrocatalytic performance for water splitting. The average crystallite size of rGO, Dy-MOF, Cr-MOF, Dy–Cr-MOF, and Dy–Cr-MOF/rGO nanocomposites are calculated to be 1.9, 10.9, 11.5, 14.7, and 23.8 nm respectively using the Debye–Scherrer Eq.

$$D = K\lambda / \beta \cos\theta \tag{8}$$

In this case, β is the FWHM of the diffraction peaks, θ is the diffraction angle, and λ is the wavelength of the x-ray[25]. Table 1 shows the XRD parameters like the rGO, Dy-MOF, Cr-MOF, Dy–Cr-MOF, and Dy–Cr-MOF/rGO lattice constants, d-spacing, lattice strain, crystallite size, and dislocation density. These values are derived from Eqs. (9), (10), and (11). Higher 2θ XRD peak values indicate that the lattice strain is increasing. Increased lattice strain results in reduced lattice parameters and, according to Bragg's law, the peak position will shift. This shows that the material is undergoing structural changes as the lattice deforms under strain.

Wavenumber (cm^{-1})	Assignment	Vibrational mode	Material(s)
3384	O–H stretching	Stretching of hydroxyl groups and adsorbed water	rGO
3376	O–H stretching	Stretching of hydroxyl groups and adsorbed water	Cr-MOF, Dy-MOF, Dy–Cr-MOF, Dy–Cr-MOF/rGO
1616–1625	C=O stretching	Asymmetric stretching of carboxylate groups	Cr-MOF, Dy-MOF, Dy–Cr-MOF, Dy–Cr-MOF/rGO
1528–1542	C–C stretching	Aromatic ring stretching	Cr-MOF, Dy-MOF, Dy–Cr-MOF, Dy–Cr-MOF/rGO
1432	C=C stretching	Sp^2 carbon skeleton of graphene	rGO, Dy–Cr-MOF/rGO
1367–1385	C–O stretching	Symmetric stretching of carboxylate groups	Cr-MOF, Dy-MOF, Dy–Cr-MOF, Dy–Cr-MOF/rGO
909	Dy-O stretching	Metal-oxygen coordination bond (Dy^{3+})	Dy-MOF, Dy–Cr-MOF, Dy–Cr-MOF/rGO
689	Cr–O stretching	Metal–oxygen coordination bond (Cr^{3+})	Cr-MOF, Dy–Cr-MOF, Dy–Cr-MOF/rGO

Table 2. FTIR peak assignments and vibrational modes of rGO, Dy-MOF, Cr-MOF, Dy–Cr-MOF, and Dy–Cr-MOF/rGO.

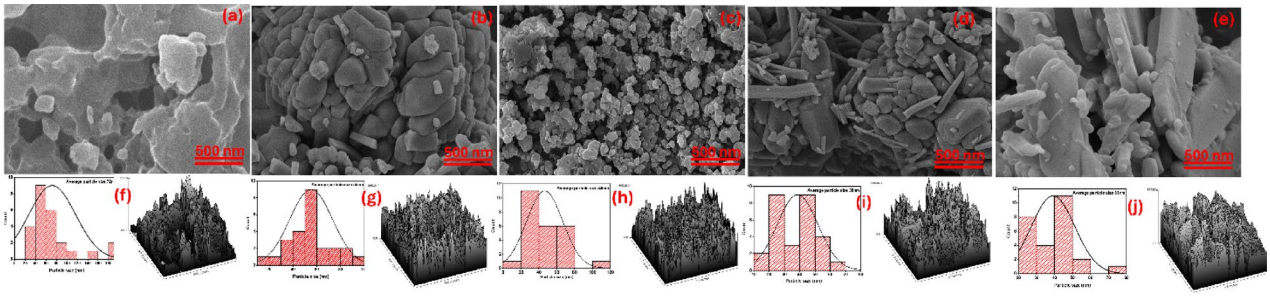

Fig. 2. SEM images of **a** rGO, **b** Dy-MOF, **c** Cr-MOF, **d** Dy–Cr-MOF and **e** Dy–Cr-MOF/rGO Histogram and Surface plot of **f** rGO, **g** Dy-MOF, **h** Cr-MOF, **i** Dy–Cr-MOF and **j** Dy–Cr-MOF/rGO.

$$Dislocation\ Density = \frac{1}{D^2} \tag{9}$$

$$Lattice\ strain = \frac{\beta}{4tan\theta} \tag{10}$$

$$d - spacing = \frac{n\lambda}{2sin\theta} \tag{11}$$

The functional groups and bonding interactions in rGO, Dy-MOF, Cr-MOF, Dy–Cr-MOF, and Dy–Cr-MOF/rGO were investigated by FTIR spectroscopy (Fig. 1b). The detailed peak assignments and corresponding vibrational modes are summarized in Table 2. The broad O–H stretching band at 3376–3384 cm^{-1} and the characteristic C=C stretching at 1432 cm^{-1} confirm the successful reduction of graphene oxide to rGO[26]. All MOF containing samples exhibit typical carboxylate vibrations (C=O at 1610–1625 cm^{-1}, C-O at 1367–1385 cm^{-1}) and aromatic C-C stretching (1528–1542 cm^{-1}), verifying coordination of BTC linker to metal centers[27]. The presence of distinct Dy–O (909 cm^{-1}) and Cr–O (689 cm^{-1}) bands in Dy-MOF, Cr-MOF, Dy–Cr-MOF, and the composite confirms the formation of the respective metal-oxygen coordination bonds[28]. In Dy–Cr-MOF/rGO, the simultaneous appearance of both Dy–O and Cr–O peaks together with the preserved graphene C=C band demonstrates successful integration of the bimetallic MOF onto the rGO support without structural degradation, thereby ensuring enhanced electrochemical properties of the final composite.

Structural differences for each material become apparent in their SEM images. From the perspective of enhanced electrocatalysis, the rough, porous, and wrinkled surface of the rGO in Fig. 2a is indicative of a considerable porosity and a good accessibility of active surfaces. Figure 2b depicts the morphology of the Dy-MOF with its small, uniform crystalline particles, which are indicative of efficient active charge dispersion, and of a limitation in the charge active sites. The larger crystalline units of the Cr-MOF shown in Fig. 2c reflects a robust framework which is positive in terms of stability. Dy–Cr-MOF shown in Fig. 2d, combines the attributes of Dy-MOF and Cr-MOF to create a bimetallic framework which, in principle, is expected to augment the electroactive catalytic property due to synergistic effects.

The Dy–Cr-MOF/rGO composite in Fig. 2e displays well-dispersed rGO sheets among the MOF particles which enhances charge transfer and active site accessibility. From the histograms and the surface plots, surface morphology and the size of the particles, which is shown in Fig. 2f and j. rGO has a 72 nm particle size with a rough texture, which enhances surface area and electro mobility, as shown in Fig. 2f. The 55 nm, which is shown in Fig. 2g, Dy-MOF also has a smooth surface which indicates a more ordered structure with efficient charge transfer. Cr-MOF in Fig. 2h has larger, more rigid framework aggregates of 46 nm which could provide stability but also provided charge active sites.

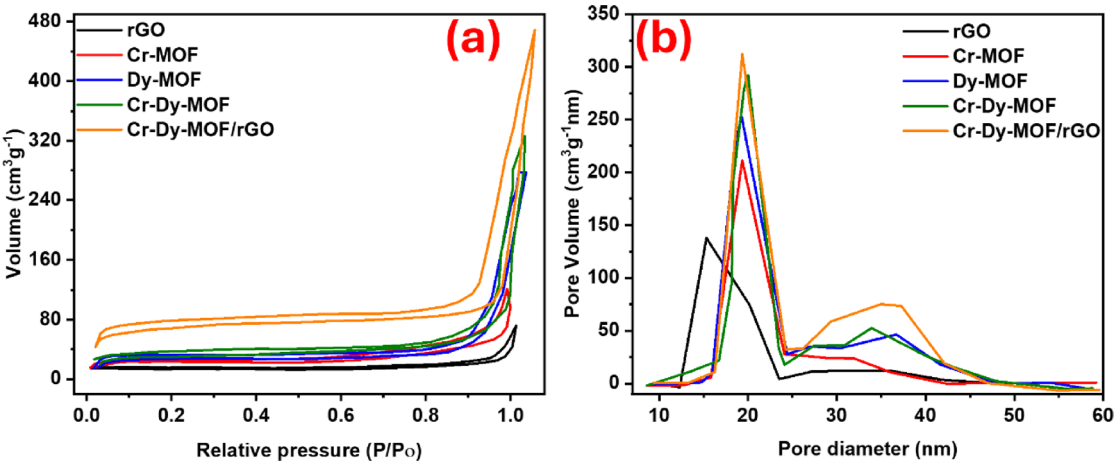

Fig. 3. BET isotherms **a** SSA and **b** Pore size of rGO, Dy-MOF, Cr-MOF, Dy–Cr-MOF and Dy–Cr-MOF/rGO.

Material	Specific Surface Area (m2/g)	Pore Size (nm)	Pore Volume (cm3/g)
rGO	71	0.96	0.017
Dy-MOF	118	0.61	0.018
Cr-MOF	275	0.26	0.018
Dy–Cr-MOF	325	0.41	0.033
Dy–Cr-MOF/GO	469	0.45	0.053

Table 3. Comparative table of BET surface area, BJH pore size, and pore volume.

The specific structural features of the Dy–Cr-MOF/rGO composite facilitate effective electrochemical water splitting. The BET surface area value remarkably improves from 71 m^2/g for rGO, to 469 m^2/g for Dy–Cr-MOF/rGO (Fig. 3(a)), meaning a significant increase. This indicates the formation of a highly porous nanocomposite. Enhancement in surface area increases the number of active catalytic sites available thus improving electrochemical performance. Figure 3 (b) illustrates the decrease in pore size from 0.96 nm (rGO) to 0.45 nm (Dy–Cr-MOF/rGO) whilst remaining in the mesopore range. Smaller pore size will not negatively affect catalytic performance, especially with respect to the more efficient ion transport to the active sites. Dy–Cr-MOF and Dy–Cr-MOF/rGO both possess a Type IV isotherm with H1/H2 loop due to their mesopore formation. rGO, in addition, to improving the mesopore formation, also enhances mass transport, critical for effective electrocatalysis. Combination of surface area, improved pore structure with rGO, improves transport of electrons in addition to mass, resulting in a greater catalytic activity for both hydrogen and oxygen evolution reactions. These enhancements in structure contribute to the excellent stability and overall catalytic performance of Dy–Cr-MOF/rGO in water splitting applications (Table 3).

Oxygen evolution reaction (OER) performance

The Cr-Dy-MOF/rGO composite demonstrates enhanced OER performance due to the collaborative interaction of rGO high conductivity and the catalytic properties of the Dy–Cr-MOF Fig. 4. The OER process requires the least amount of energy to start with this material, as evidenced by the lowest potential onset of 2.30 V. Other materials, including Dy–Cr-MOF, Dy-MOF, Cr-MOF, and rGO showed higher values. The lowest Tafel slope of Dy–Cr-MOF/rGO at 42 mV dec^{-1} reflects swift reaction kinetics and efficient charge transfer, and this is much higher than the Tafel slopes of the other materials, which ranged from 73 to 102 mV dec^{-1}. The overpotential of 164 mV at 10 mA cm^2 for Dy–Cr-MOF/rGO is further proof of its enhanced catalytic activity. The lowest charge transfer resistance (EIS) of Dy–Cr-MOF/rGO at 5.77 Ω, which justifies the faster electron transport and superior OER performance. For more than 50 h of uninterrupted operation, the performance of Dy–Cr-MOF/rGO is stable, and it is remarkable without significant decrease. The combination of the bimetallic Dy–Cr-MOF with rGO conductivity increases efficiency by improving electron transport and kinetics while having more active sites. Moreover, the Dy–Cr-MOF/rGO surpassed all materials in Turnover Frequency (TOF), which was 1.36 s^{-1}, denoting the highest degree of electrocatalytic activity. The compatibility of Dy–Cr-MOF/rGO composites with advanced materials for water-splitting applications can be attributed to their efficient performance in the OER, excellent conductivity, efficient charge transfer, and remarkable stability.

Mechanism of OER

The OER on the Cr-Dy-MOF/rGO composite begins with the adsorption of water onto the catalyst surface. This is due to the improved surface area and porosity of the Cr-Dy-MOF framework. As shown in the SEM and BET analyses, these features along with the Cr and Dy metal sites, enhance water molecule adsorption and activation,

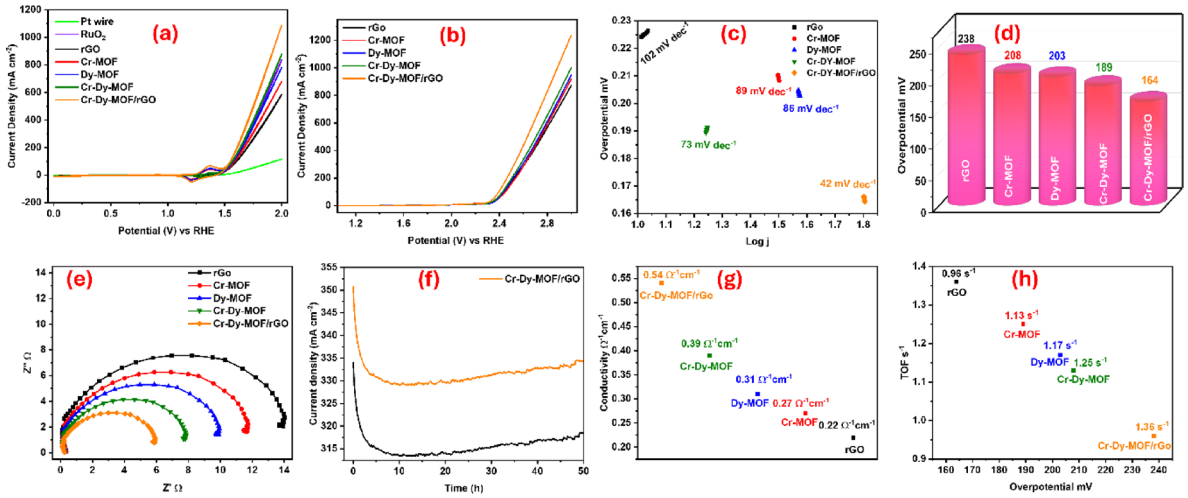

Fig. 4. **a** CV curves, **b** LSV curves, **c** Tafel slope, **d** Overpotential, **e** EIS, **f** Chronoamperometry, **g** Conductivity, **h** TOF of rGO, Dy-MOF, Cr-MOF, Dy–Cr-MOF and Dy–Cr-MOF/rGO in basic media.

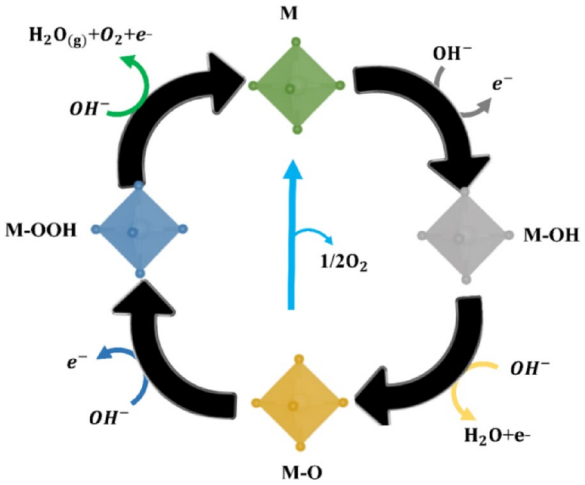

Scheme 3. Mechanism of OER.

assisting in the formation of hydroxyl (OH) intermediates. The Cr and Dy ions within the MOF framework also promote in the stabilization of these oxygen intermediates, thereby enhancing the catalytic activity. Eventually, the intermediates encounter each other to form an O = O bond, thus releasing oxygen gas and generating protons and electrons Scheme 3. The role of rGO support is pivotal as it enhances electron transport through a conductive to facilitate effective charge transfer. Thus, the Cr-Dy-MOF structure efficiently enhances OER through optimized adsorption of intermediates[29,30].

$$M + OH^- \rightarrow MOH + e^- \quad \text{Tafel slope} = 120\text{mVdec}^{-1} \tag{12}$$

$$MOH + OH^- \rightarrow H_2O + MO + e^- \quad \text{Tafel slope} = 60\text{mVdec}^{-1} \tag{13}$$

$$\text{MO} + \text{MO} \rightarrow 2\text{M} + \text{O}_2 \tag{14}$$

$$\text{MO} + \text{OH}^- \rightarrow \text{MOOH} + \text{e}^- \quad \text{Tafel slope} = 40\text{mVdec}^{-1} \tag{15}$$

$$\text{MOOH} + \text{OH}^- \rightarrow \text{M} + \text{O}_2 + \text{H}_2\text{O} + \text{e}^- \quad \text{Tafel slope} = 15\text{mVdec}^{-1} \tag{16}$$

Hydrogen evolution reaction (HER) performance

The hydrogen evolution reaction (HER) performance of Dy–Cr-MOF/rGO improves significantly compared to Dy-MOF, Cr-MOF, Dy–Cr-MOF, and rGO Fig. 5. HER performance of the catalyst is also indicative of having the fastest reaction kinetics and charge transfer, recognized by the lowest Tafel slope of 32 mV dec^{-1}. Dy–Cr-MOF/rGO also shows the lowest overpotential (158 mV at 10 mA cm^2) and less energy is needed to drive the

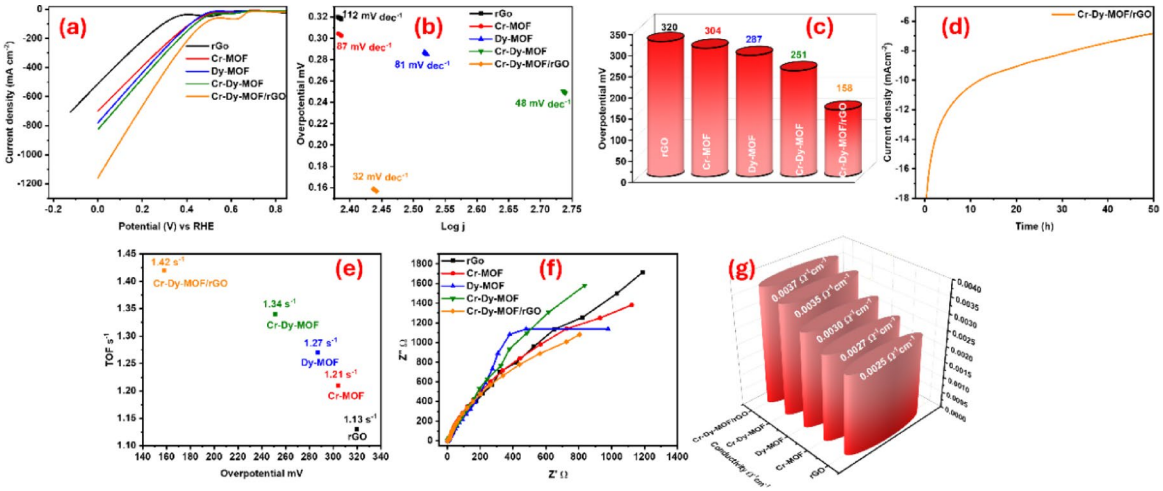

Fig. 5. **a** LSV curves, **b** Tafel slope, **c** Overpotential, **d** Chronoamperometry, **e** TOF, **f** EIS, **g** Conductivity of rGO, Dy-MOF, Cr-MOF, Dy–Cr-MOF and Dy–Cr-MOF/rGO in basic media.

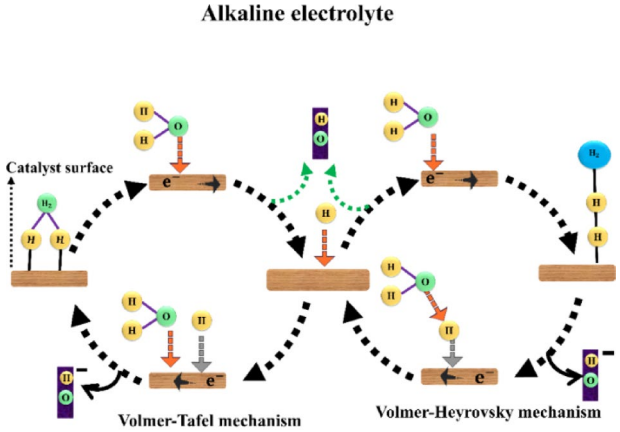

Scheme 4. Mechanism of HER.

HER process, which is indication of its active catalysis. The Cr and Dy dual metal synergy in the MOF structure is critical to the optimization of hydrogen storage dynamics but active hydrogen rGO scaled Dy–Cr-MOF supports in energy transport, decreasing the total energy barrier. The conductive rGO network is crucial in resource efficient transport and in preventing charge carrier recombination but preventing process instability of the HER. The long-term stability tests conducted over 50 crucibles confirm the practical utility and durability of Dy–Cr-MOF/rGO as process active stability is preservation performance is incredible. The catalyst's performance also contains the better turnover frequency (TOF) of 1.42 s^{-1} proving effective hydrogen generation per active site. Electrochemical impedance spectroscopy (EIS) confirms enhanced charge transfer and reaction kinetics by a low charge transfer resistance (816.54 Ω) proving the highly conductive characteristic of the supplied mass and low resistance contributed largely to the released mass in the process of hydrogen production. Having a larger surface area and a more porous structure allows the Dy–Cr-MOF to more effectively adsorb and activate the reactants to accelerate the HER process. Dy–Cr-MOF/rGO combines all of the required attributes to perform well as an HER catalyst: excellent conductivity and stability, and the high availability of active sites. This catalyst also surpasses the performance of the individual components, such as pure MOFs and rGO.

Mechanism of HER

HER involves various steps where protons undergo reduction and hydrogen gas is produced. Dy–Cr-MOF/rGO, the process can be reduced to the following steps Scheme 4: The first stage in HER is the protons (H^+) adsorbing onto the catalyst's surface. The Cr and Dy metal sites inside the MOF structure act as active sites in Cr–Dy-MOF/rGO to assist proton adsorption from the electrolyte. At the catalyst surface upon adsorption by electrons, the protons are transformed to hydrogen atoms (H). This stage of the proton-coupled electron transfer (PCET) process sends an electron from the electrode to the adsorbed proton, producing a hydrogen atom (H

intermediate). On the catalyst, this creates an intermediary*. Desorb the hydrogen atom in the last stage using the catalyst surface; this then reacts to generate molecular hydrogen (H_2) and is then released. The H–H link has to be broken in order to move forward. While electron transport is boosted by the rGO support, the Cr and Dy metal centers promote proton adsorption and activation in Cr–Dy-MOF/rGO, so producing effective proton reduction and hydrogen evolution. While the high conductivity of rGO reduces charge transfer resistance, therefore enabling an effective HER process, the metal sites in the MOF framework stabilize the hydrogen intermediates[31,32]. The rGO support dramatically lowers charge-transfer resistance and boosts electron supply, while Cr/Dy metal centers stabilize H intermediates, yielding a high j_0 of up to 1.2 mA cm^{-2} through enhanced active-site density at the heterojunction interface, enabling highly efficient HER.

$$H_2O + M + e^- \rightarrow MH_{ads} + OH^- \quad \text{Volmer Step} \tag{17}$$

$$MH_{ads} + H_2O + e^- \rightarrow M + H_2 + OH^- \quad \text{Heyrovsky step} \tag{18}$$

$$2\,MH_{ads} \rightarrow 2M + H_2 \quad \text{Tafel slop} \tag{19}$$

The electrochemical double-layer capacitance (Cdl) was measured to determine the electrochemical active surface area (ECSA) of the catalysts. A larger Cdl value indicates a bigger surface area, enhancing electron and ion transfer for effective water splitting. As shown in Fig. 6, rGO has a smaller Cdl value of 1.5 mF, while Dy-MOF shows a Cdl of 2.7 mF (ECSA of 67.5). Cr-MOF further improves surface area with a Cdl of 3.4 mF and ECSA of 85. The Dy–Cr-MOF composite has a Cdl of 4.5 mF and an ECSA of 112.5, showing a synergistic increase in surface area. The Dy–Cr-MOF/rGO composite achieved the highest Cdl value compared to 11.4 mF with an ECSA of 285 due to the hybrid of the porous Dy–Cr-MOF with conductive rGO. This combination increases the Dy–Cr-MOF/rGO effective surface area and Dy–Cr-MOF/rGO conductivity demonstrating superb effectiveness for the Dy–Cr-MOF/rGO for the HER and OER processes and thus improving water splitting (Table 4).

Two electrode systems

In a two-electrode water splitting experiment, different parameters used in the electrochemistry of the performance testing of the electrode materials geared for the hydrogen evolution reaction (HER) and oxygen evolution reaction (OER) are emphasized. This begins with the cyclic voltammetry (CV) at Fig. 7 (a) which shows the current response over a range of applied voltages with respect to the electrochemical characterization of the electrodes. The CV curve illustrates the commencement of reactions, e.g., OER and HER, with peaks separated offering information on the material's kinetics and efficiency. Anodic linear sweep voltammetry (LSV) is focusing on the OER performance of the anode. In Fig. 7 (b) anodic LSV curve depicts current density vs. applied voltage, with current density and the onset potential being crucial markers of the efficiency of the electrode towards oxygen evolution. whereas cathodic linear sweep voltammetry (LSV) is utilized to examine the HER performance on the cathodic electrode. This information displays the present response of hydrogen evolution and gives comparable insights as anodic LSV but for the cathodic process. In Fig. 7(d) Tafel slope values represent the reaction kinetics. The Tafel slope for OER is 108 $mVdec^{-1}$, whereas the Tafel slope of the HER is 87 $mVdec^{-1}$. These data suggest that the HER process has a faster reaction rate than OER, since a smaller Tafel slope implies a more effective electrochemical reaction of lower activation energy. This gap in Tafel slopes represents the underlying differences in the two reactions kinetics, with HER usually more favorable under normal circumstances than OER. The overpotential values also represent the performance of the electrodes. In the case of OER, there is a need of 522 mV to the reaction for a specific current density, reflecting the energy barrier that should be overcome in order for the reaction to take place successfully. In the case of HER, the overpotential is smaller, suggesting that less energy is required to drive the process of hydrogen evolution than oxygen evolution. This shows that the material is more effective for HER, since less voltage is required to create hydrogen. Charge transfer resistance (Rct) values acquired from electrochemical impedance spectroscopy (EIS) also give information about electrochemical processes. In Fig. 7 (f-g) charge transfer resistance is 31 Ω

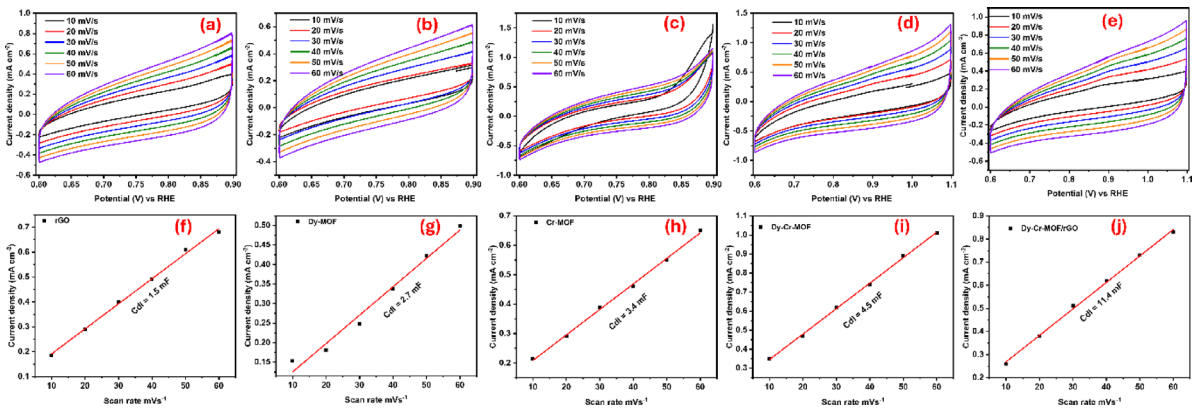

Fig. 6. **a–e** CV curves at various scan rates and **f–j** Cdl values of rGO, Dy-MOF, Cr-MOF, Dy–Cr-MOF and Dy–Cr-MOF/rGO in basic media.

Sample	Overpotential at 10 mA/cm² (V)	Tafel Slope (mV/dec)	Activity	Reference
P, N-PCCo/rGO	39 235	88.9 110	HER OER	33
CoP/rGO	105 340	50 66	HER OER	34
V-Nix: Fey MOF/GO	90 210	150 97	HER OER	35
$CoCr_2O_4$/rGO	274	. 53	HER OER	36
Mesh-CrFe-CoP NSs	103.7 256.4	90.9 55.9	HER OER	19
$Ni_{0.85}Se$/RGO/CNTs	165 232	98 64	HER OER	37
Cr–Ni_3FeN/Ni@N-GTs	88 262	103 32	HER OER	38
La-doped CoMoP	49 250	127.7 88.9	HER OER	39
Ni/(α,β)-NiS MOF@CNT	123 244	50.8 47.2	HER OER	40
$NiFe_2O_4$@N/rGO-800	252 157	51.2 49.7	OER HER	41
Co/Mo-rGO	420	126	OER	42
FeDy@MOF-Ni/CC	251	52.1	OER	15
Ni_xP/rGO $NiFe_2O_4$@N/rGO-800	142 260 157 252	58 62 94.7 56.5	HER OER HER OER	43 44
RuNi-rGO@MNCs-$_2$	28	35	HER OER	45
Cr-Dy MOF/rGO	164 158	32 42	HER OER	Current study

Table 4. Comparison table between designed electrode material and published literature.

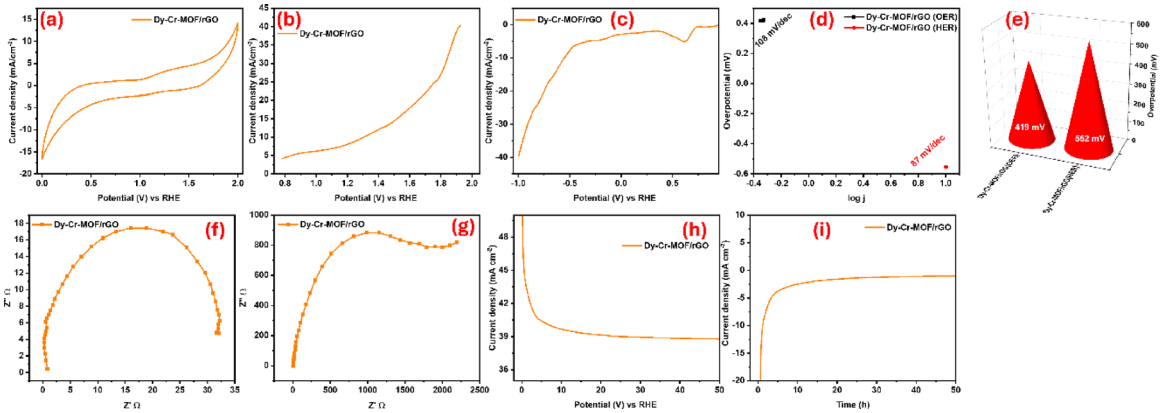

Fig. 7. Two Electrode water splitting analysis **a** CV, **b** anodic LSV, **c** cathodic LSV, **d** Tafel analysis, **e** overpotential for HER and OER, **f** EIS of OER, **g** EIS of HER, **h** Chronoamperometric of OER, **i** Chronoamperometric of HER of Cr-Dy-MOF/rGO.

for OER, but for HER it is substantially greater at 2245 Ω. Lower Rct values for OER indicate that the material facilitates more efficient charge transfer during the oxygen evolution reaction; however, higher Rct values for the HER demonstrate that the hydrogen evolution reaction is more sluggish and resistant and will need further optimization to alleviate this resistance and improve overall performance. In Fig. 7 (h-i) chronoamperometric stability experiments reveal that the material displays steady performance for both OER and HER after 50 h. This shows that the electrodes retain their catalytic activity and efficiency over a long length of time, demonstrating good durability and long-term stability for both processes. The capacity to retain performance over such a long time is critical for real-world applications, where electrodes must work for longer periods without substantial degradation.

Conclusion

Hydrothermally synthesized Dy–Cr-MOF/rGO heterojunction exhibits outstanding bifunctional electrocatalytic performance in alkaline media, achieving lowest overpotentials of only 158 mV (HER) and 164 mV (OER) at 10 mA cm^{-2} with remarkably fast kinetics (Tafel slopes of 32 and 42 mV dec^{-1}, respectively). This superior activity originates from the synergistic coupling of highly dispersed Dy–Cr-MOF nanoparticles on conductive rGO nanosheets, which prevent aggregation, maximizes active-site exposure, and dramatically enhances charge-transfer efficiency. Composite demonstrates excellent practical viability: in a two-electrode alkaline electrolyzer, it delivers 10 mA cm^{-2} at a cell voltage of just 1.62 V and maintains stable operation for over 50 h with negligible degradation, outperforming many state-of-the-art noble-metal-free catalysts. It's simple, scalable hydrothermal synthesis, low-cost precursors, and compatibility with nickel-foam electrodes make it highly promising for large-scale green hydrogen production. These results establish Dy–Cr-MOF/rGO as a competitive, earth-abundant platform for next-generation renewable energy conversion technologies.

Data availability

All data generated or analyzed during this study are included in this published article [and its supplementary information files.

Received: 28 October 2025; Accepted: 18 December 2025
Published online: 24 December 2025

References

1. Anandhababu, G., Huang, Y., Babu, D. D., Wu, M. & Wang, Y. Oriented growth of ZIF-67 to derive 2D porous CoPO nanosheets for electrochemical-/photovoltage-driven overall water splitting. *Adv. Funct. Mater.* **28**, 1706120 (2018).
2. Kamran, M. & Turzyński, M. Exploring hydrogen energy systems: A comprehensive review of technologies, applications, prevailing trends, and associated challenges. *J. Energy Storage*. **96**, 112601 (2024).
3. Ganesan, A., Kayalvizhi, B., Hemalatha, P., Oh, T. H., Ramasundaram, S. & Arunachalam, K. P. Interface-driven electrochemical behavior of NbOxC-based materials for high performance oxygen evolution reaction. *J. Electroanal. Chem.* **999**, 119562 (2025).
4. Tan, Y. et al. Carbon-coated MoSe2/Mo2CTx (MXene) heterostructure for efficient hydrogen evolution. *Mater. Sci. Eng. B.* **271**, 115239 (2021).
5. Qian, Q. et al. Recent advancements in electrochemical hydrogen production via hybrid water splitting. *Adv. Mater.* **36**, 2306108 (2024).
6. Zhang, B. et al. Designing MOF nanoarchitectures for electrochemical water splitting. *Adv. Mater.* **33**, 2006042 (2021).
7. Zhou, Q. et al. Co3S4-pyrolysis Lotus fiber flexible textile as a hybrid electrocatalyst for overall water splitting. *J. Energy Chem.* **89**, 336–344 (2024).
8. Wen, Q., Zhao, Y., Liu, Y., Li, H. & Zhai, T. Ultrahigh-current-density and long-term-durability electrocatalysts for water splitting. *Small* **18**, 2104513 (2022).
9. Wang, K., Hui, K. N., San Hui, K., Peng, S. & Xu, Y. Recent progress in metal–organic framework/graphene-derived materials for energy storage and conversion: design, preparation, and application. *Chem. Sci.* **12**, 5737–5766 (2021).
10. Xu, G., Zhu, C. & Gao, G. Recent progress of advanced conductive metal–organic frameworks: precise synthesis, electrochemical energy storage applications, and future challenges. *Small* **18**, 2203140 (2022).
11. Udayakumar, A., Dhandapani, P., Ramasamy, S., Yan, C. & Angaiah, S. Recent developments in noble metal–based hybrid electrocatalysts for overall water splitting. *Ionics* **30**, 61–84 (2024).
12. Noor, T., Yaqoob, L., &, Iqbal, N. Recent advances in electrocatalysis of oxygen evolution reaction using noble-metal, transition-metal, and carbon-based materials. *ChemElectroChem* **8**, 447–483 (2021).
13. Naresh, B., Sreekanth, T., Prasad, K., Yoo, K. & Kim, J. Mg and cr doped ZnO nanoparticles for oxygen evaluation reaction. *Surf. Interfaces*. **56**, 105437 (2025).
14. Aman, S. et al. An ultrafast oxygen evolution reaction catalyzed by an amorphous Nickel–Dysprosium-based electrocatalyst with extraordinary Spatial morphology. *J. Solgel Sci. Technol.* **106**, 226–235 (2023).
15. Wan, Z. et al. Dissolution-regrowth of hierarchical Fe-Dy oxide modulates the electronic structure of nickel-organic frameworks as highly active and stable water splitting electrocatalysts. *Chin. J. Catal.* **41**, 1745–1753 (2020).
16. Alharbi, F., Alahmari, S. D., Aman, S., Dahshan, A. & Henaish, A. Developing TiCo2O4 spinel based on rGO nanosheet to enhance electrochemical performance of OER activity. *J. Electroanal. Chem.* **963**, 118299 (2024).
17. Nagarani, S. et al. Well-organized metal-free chemically reduced graphene oxide sheets as electrocatalysts for enhanced oxygen reduction reactions in alkaline media. *Mater. Lett.* **357**, 135705 (2024).
18. Raja, A., Son, N., Swaminathan, M. & Kang, M. Electrochemical behavior of heteroatom doped on reduced graphene oxide with RuO2 for HER, OER, and supercapacitor applications. *J. Taiwan Inst. Chem. Eng.* **138**, 104471 (2022).
19. Sun, S. et al. Iron and chromium co-doped Cobalt phosphide porous nanosheets as robust bifunctional electrocatalyst for efficient water splitting. *Nanotechnology* **33**, 075204 (2021).
20. Ma, Y. et al. Hydrangea flower-like nanostructure of dysprosium-doped Fe-MOF for highly efficient oxygen evolution reaction. *Rare Met.* **41**, 1–7 (2022).
21. Ma, Y. et al. Hydrangea flower-like nanostructure of dysprosium-doped Fe-MOF for highly efficient oxygen evolution reaction. *Rare Met.* **41**, 844–850 (2022).
22. Junaid, A. et al. Developing Ag3VO4@ ZnO electrode material for efficient oxygen evolution reaction showcasing its potential for sustainable energy applications. *Fuel* **379**, 133029 (2025).
23. Meng, J., Li, F., Li, T. & Cao, W. Coating polyurethane sponge with Dy-MOF for efficient oil–water separation in complex environments. *Appl. Surf. Sci.* **614**, 156183 (2023).
24. Zhang, L., Li, F., Ren, J., Ma, L. & Li, M. Preparation of metal organic frameworks MIL-101 (Cr) with acetic acid as mineralizer. *IOP Conf. Ser.: Earth Environ. Sci.* 042038 (2018).
25. Hameed, M. A. & Harbbi, K. H. Studying the change in the dislocation density and the burger vector when the temperature changes using the method of analysis X-Ray diffraction Patterns, Ibn AL-Haitham. *J. Pure Appl. Sci.* **38**, 161–173 (2025).
26. Alam, S. N., Sharma, N. & Kumar, L. Synthesis of graphene oxide (GO) by modified hummers method and its thermal reduction to obtain reduced graphene oxide (rGO). *Graphene* **6**, 1 (2017).
27. Nisa, M. U. et al. CdSe supported SnO2 nanocomposite with strongly hydrophilic surface for enhanced overall water splitting. *Fuel* **321**, 124086 (2022).
28. Han, J. J., Yan, Q., Chen, Z., Wang, Z. & Chen, C. Application of Cr-metal organic framework (MOF) modified polyaniline/graphene oxide materials in supercapacitors. *Ionics* **28**, 2349–2362 (2022).

29. Li, L., Wang, P., Shao, Q. & Huang, X. Metallic nanostructures with low dimensionality for electrochemical water splitting. *Chem. Soc. Rev.* **49**, 3072–3106 (2020).
30. Liu, Y. et al. Research progress of oxygen evolution reaction catalysts for electrochemical water splitting. *ChemSusChem* **14**, 5359–5383 (2021).
31. Ding, X. et al. Ni3N–CeO2 heterostructure bifunctional catalysts for electrochemical water splitting. *Adv. Funct. Mater.* **33**, 2306786 (2023).
32. He, Y., Liu, W. & Liu, J. MOF-based/derived catalysts for electrochemical overall water splitting. *J. Colloid Interface Sci.* **661**, 409–435 (2024).
33. Zhao, W. et al. Metal-Organic-Framework-derived Co nanoparticles embedded in P, N-Dual-doped porous Carbon/rGO catalyst for water splitting and oxygen reduction. *ChemNanoMat* **8**, e202200225 (2022).
34. Jiao, L., Zhou, Y. X. & Jiang, H. L. Metal–organic framework-based CoP/reduced graphene oxide: high-performance bifunctional electrocatalyst for overall water splitting. *Chem. Sci.* **7**, 1690–1695 (2016).
35. Gopi, S. et al. Bifunctional electrocatalysts for water splitting from a bimetallic (V doped-NixFey) Metal–Organic framework MOF@ graphene oxide composite. *Int. J. Hydrog. Energy*. **47**, 42122–42135 (2022).
36. Jabeen, S. et al. Preparation of nano-composite of CoCr2O4 with rGO by solvothermal method for water splitting. *Diam. Relat. Mater.* **154**, 112167 (2025).
37. Pei, H., Liu, G., Guo, R., Liu, N. & Mo, Z. A novel efficient dual-functional electrocatalyst for overall water splitting based on Ni0.85Se/RGO/CNTs nanocomposite synthesized via different nickel precursors. *Int. J. Hydrog. Energy*. **47**, 35227–35240 (2022).
38. Zhou, Q. et al. Chromium doping and in-grown heterointerface construction for modifying Ni3FeN toward bifunctional electrocatalyst toward alkaline water splitting. *Int. J. Hydrog. Energy*. **48**, 15921–15933 (2023).
39. Wang, J. et al. Facilely constructing three-dimensional porous La2O3 modified Co/NC composite with modulated electron structure as excellent electrocatalyst for water splitting. *Int. J. Hydrog. Energy*. **61**, 265–274 (2024).
40. Srinivas, K. et al. Constructing Ni/NiS heteronanoparticle-embedded metal–organic framework-derived nanosheets for enhanced water-splitting catalysis. *ACS Sustain. Chem. Eng.* **9**, 1920–1931 (2021).
41. Cao, L., Li, Z., Su, K., Zhang, M. & Cheng, B. Rational design of Hollow oxygen deficiency-enriched NiFe2O4@ N/rGO as bifunctional electrocatalysts for overall water splitting. *J. Energy Chem.* **54**, 595–603 (2021).
42. Zhao, L. et al. One-pot hydrothermal synthesis of bifunctional Co/Mo-rGO efficient electrocatalyst for HER/OER in water splitting. *Catal. Lett.* **154**, 5294–5302 (2024).
43. Tazeen, Z. et al. A decade of breakthroughs: MOF-graphene oxide catalysts for water splitting efficiency. *Rev. Inorg. Chem.* **305**, 338–348 (2025).
44. Raj, R., Paswan, S. K., Kumar, L., Prasad Singh, G. & Haldar, K. K. Ti3C2T X nanosheet/NiFe2O4 nanoparticle composites for electrocatalytic water splitting. *ACS Appl. Nano Mater.* **8**, 1649–1662 (2025).
45. Zhang, C. et al. Improved electrochemical water splitting by runi nanoparticles supported on rGO@ mesoporous N-doped carbon nanosheets. *J. Alloys Compd.* **937**, 168334 (2023).

Acknowledgements

The authors extend their appreciation to the Deanship of Research and Graduate Studies at King Khalid University for funding this work through the Large Research Project under grant number RGP2/41/46.

Author contributions

Khadija-tul-Kubra, Ali Junaid: Investigation, Methodology, Writing - Review & editing. Faiqa Noreen, Aymen Shahsawar : Investigation, Validation, Saif Ullah: Validation, Data Curation, Software. Abdullah K. Alanazi, Magdi E. A. Zaki, Sobhi M. Gomha: Investigation, Validation, Funding acquisition. Mohamed A. Salem: Validation, Revision, Review & editing. Syed Imran Abbas Shah, Zahid Shafiq: Conceptualization, Supervision, Writing - Review & editing.

The authors extend their appreciation to the Deanship of Research and Graduate Studies at King Khalid University for funding this work through the Large Research Project under grant number RGP2/41/46.

Declarations

Competing interests

The authors declare no competing interests.

Additional information

Supplementary Information The online version contains supplementary material available at https://doi.org/10.1038/s41598-025-33457-x.

Correspondence and requests for materials should be addressed to S.I.A.S., S.M.G. or Z.S.